Monitoring the sodiation mechanism of anatase TiO$_2$ nanoparticles-based electrodes for sodium-ion batteries by *operando* XANES measurements

Andreas Siebert,[1] *Xinwei Dou,*[2,3] *Raul Garcia-Diez,*[1] *Daniel Buchholz,*[2,3] *Roberto Félix,*[1] *Evelyn Handick,*[1] *Giorgia Greco,*[4] *Ivana Hasa,*[2,3] *Regan G. Wilks,*[1,5] *Stefano Passerini,*[2,3] *Marcus Bär*[1,5,6,7]

[1] Interface Design, Helmholtz-Zentrum Berlin für Materialien und Energie GmbH (HZB), Berlin, Albert-Einstein-Strasse 15, 12489 Germany

[2] Helmholtz Institute Ulm (HIU), Helmholtzstrasse 11, D-89081 Ulm, Germany

[3] Karlsruhe Institute of Technology (KIT), P.O. Box 3640, D-76021 Karlsruhe, Germany

[4] Institute for Nanospectroscopy, Helmholtz-Zentrum Berlin für Materialien und Energie GmbH (HZB), Albert-Einstein-Strasse 15, 12489 Berlin, Germany

[5] Energy Materials In-Situ Laboratory Berlin (EMIL), Helmholtz-Zentrum Berlin für Materialien und Energie GmbH, Albert-Einstein-Strasse 15, 12489 Berlin, Germany

[6] Helmholtz-Institute Erlangen-Nürnberg for Renewable Energy (HI ERN), Fürther Strasse 248, 90429 Nürnberg, Germany

[7] Department of Chemistry and Pharmacy, Friedrich-Alexander-Universität Erlangen-Nürnberg,

Nikolaus-Fiebiger-Strasse 10, 91058 Erlangen, Germany

Abstract

Anatase TiO_2 represents an attractive electrode material for application in sodium-ion batteries due to its relatively low cost, high environmental compatibility, high intrinsic safety, conferred by the relatively high operating voltage, and satisfactory theoretical capacity. Nonetheless, a comprehensive understanding of the Na uptake and release mechanism is still missing, which is crucial for a further insight-driven optimization of the electrode material. This work presents for the first time an extensive *operando* X-ray absorption near-edge structure spectroscopy (XANES) study at the Ti K-edge of a TiO_2 anatase nanoparticle-based electrode, aiming at unraveling the structural evolution and consequent Ti oxidation state and coordination changes upon sodiation and following de-sodiation. By using two approaches, i.e. an analytical fit and principal component analysis (PCA) with a linear combination analysis (LCA) to the evaluation of the *operando* data, this study reveals the amount of irreversible and reversible Na^+ inserted upon cycling. In addition, a change of the Ti coordination during the first cycle is monitored, observing a decrease of the original 6-coordinated symmetry. Simultaneously, the irreversible loss of the nanoparticle structural ordering due to the effect of initial Na insertion in the anatase lattice is detected. These results support some of the (*ex situ*) findings reported previously and give a more comprehensive picture of the highly discussed sodiation mechanism of TiO_2-based anodes under more realistic operating conditions.

1. Introduction

Sodium-ion batteries (SIBs) represent a promising, not necessarily competing, alternative electrochemical energy storage technology to lithium-ion batteries (LIBs). The interest towards SIBs is mainly driven by the abundance, homogeneous distribution, and low cost of the foreseen employed raw materials with respect to LIBs, leading to lower economic and geopolitical impact.[1,2]

Several materials have been proposed as promising negative electrode (anode) materials for application in SIBs.[3,4] Among them, carbon and titanium based compounds, such as hard carbon[5] and titanium oxides[6] have attracted large attention due to their nontoxicity, low cost, and environmentally friendliness. Theoretically, up to one equivalent of lithium is inserted per mol of TiO_2 corresponding to a theoretical specific capacity of about 330 mAh·g^{-1}.[7] However, in the case of sodium only around 0.5 equivalent of Na per mol of TiO_2 are inserted, resulting in a reversible capacity of 150 mAh·g^{-1}.[8] TiO_2 has several allotropes characterized by different crystalline structures, such as the anatase tetragonal phase (space group I41/amd), the rutile tetragonal phase (space group P42/mnm), and the brookite orthorhombic phase (space group Pbca), each of them characterized by different electrochemical properties according to their morphology and structure.[9–13]

Among these structures, the most promising results in terms of specific capacity and cycle life have been obtained by employing anatase TiO_2.[8,9,11–20] Additionally, the nanostructuring of the TiO_2 material has proven to be beneficial for the battery performance in terms of conductivity and specific capacity.[13,16] For instance, it was shown that reducing the size of the anatase TiO_2 nanoparticles leads to higher amounts of reversible inserted and extracted sodium ions per

formula unit TiO_2.[16] In another study, it was shown that the size and morphology of these nanoparticles remains unchanged upon sodiation,[21] while the detailed structural and electronic changes of the anatase TiO_2 upon Na uptake and the consequent structural rearrangements are still not well understood, especially in relation to the first irreversible capacity loss, nearly 40 %, observed during the initial sodiation process.[8,13]

Contradicting results about the processes underlying the sodiation mechanism have been proposed, especially in relation to the retention of the anatase structure. Reported X-ray diffraction (XRD) and Raman measurements describe an amorphization of the anatase TiO_2-based electrode material upon sodiation,[8,11,22–25] with a loss of the long range order of the anatase structure, not observed in other studies.[20,26,27] Furthermore, different (local) crystal symmetries have been proposed for the sodiated titanium oxide phase: a retention of the local anatase structure,[27] the formation of an orthorhombic $NaTi_2O_4$ phase,[26] or a change towards a rhombohedral $R\bar{3}m$ phase,[22] all of which contain titanium in a 6-coordinated environment. However, more recent work suggests a change of the coordination of titanium upon sodiation towards a lower 5-coordinated structure.[23] Although most of the previous studies suggest that the Ti^{4+}/Ti^{3+} redox reaction is the active redox couple upon sodium insertion,[8,23,26,28] the amounts of inserted sodium per formula unit of TiO_2 differ and are rarely reported, especially for the irreversible inserted sodium.

As an example, electrochemical insertion of sodium in commercial TiO_2 nanoparticles was reported to involve the initial formation of an intermediate sodium titanate, its subsequent disproportionation into a new sodium titanate phase with a lower sodium content (about 0.25 Na^+ per formula unit TiO_2), and the final formation of metallic titanium and sodium superoxides.[8] This report was later corrected based on *ex-situ* XANES investigation, excluding the formation

of metallic Ti.[23] Nonetheless, among these processes, only the (de-)insertion of sodium ions from the sodium titanate phase appears to be reversible.

The above-mentioned results clearly indicate that the detailed sodiation mechanism of TiO_2 is still unclear and heavily debated. As a matter of the fact, despite several investigations having been carried out, a clear correlation between the (de-)sodiation process and the changes in the electronic and local structures of TiO_2 is still missing. Furthermore, *operando* investigations of the system are scarce,[13] creating an additional uncertainty to the so far proposed mechanisms.

X-ray absorption near-edge structure spectroscopy (XANES) is a suitable and powerful tool to study the electronic and molecular orbital changes of anatase TiO_2 upon cycling. XANES is element-specific and it probes the local unoccupied partial density of electronic states of materials. In this context in particular, XANES at the Ti K-edge is able to probe the Ti atoms and the nearest neighbors in the oxide environment. In addition to its high sensitivity to the coordination state of Ti and the crystalline structure of TiO_2,[23,29–34] XANES is a suitable tool for the detection of the Ti valence state changes upon cycling.[29,30,35]

Ex-situ XANES analysis can offer useful insights in the reaction mechanism of battery materials, however, postmortem analysis on electrodes recovered from disassembled electrochemical cell and eventual rinsing steps required to remove electrolyte residuals, can affect and modify the chemical, structural and morphological properties of the investigated samples. For this reason, *operando* X-ray spectroscopy is gaining considerable attention in the characterization of battery anodes,[36,37] though its implementation for the investigation of relevant SIB materials is still technically challenging due to a short X-ray attenuation length, and/or missing theoretical background to interpret the spectroscopic results. Despite the challenging application of *operando* X-ray spectroscopy on SIB materials, in the specific case of TiO_2,

several studies already exist in literature and constitute an invaluable database of information on the structural properties of a variety of polymorphs of TiO_2. An elegant and comprehensive study of the coordination chemistry and disorder in oxide compounds and the medium range environment around Ti in oxide glasses has been reported by Farges et al. evaluating the coordination state of Ti according to the pre-edge peak maximum intensity and position of Ti K-edge XANES spectra.[32,34] It was shown that the largest pre-edge peak intensity is found for 4-coordinated Ti ([4]Ti) while the lowest intensity is typically observed for 6-coordinated Ti ([6]Ti), with 5-coordinated Ti ([5]Ti) resulting in an intermediate intensity. The pre-edge position changes from lower photon energies for [4]Ti towards higher excitation energies for [6]Ti, again with [5]Ti in between.[34] Besides the effect of coordination, the pre-edge peak position and intensity can also be affected by the oxidation state, as a shift of around 2 eV was reported for a change in valency from Ti^{+4} to Ti^{+3}.[29] Additionally the pre-edge peak maximum intensity of tetragonal 5-coordinated transition metal species was observed to decrease with the amount of occupied 3d states[38] and a similar effect was shown comparing Fe K-edge XANES spectra of 4- and 5-coordinated Fe^{+2} and Fe^{+3} species.[39]

In this paper, we examine the effects of (de-)sodiation on the chemical, electronic, and structural properties of a model anode electrode, consisting of stoichiometric TiO_2 nanoparticles. Changes are investigated by analyzing the Ti K-edge XANES spectral features during cell operation (i.e., during (dis-)charging cycles) by means of an analytical fit and a PCA/LCA approach. These investigations represent our current state of evaluation, giving new information about the sodiation mechanism in TiO_2-based anodes. Additional investigations using a multivariate curve resolution (MCR) and density functional theory (DFT) approach are in progress and will be presented in a follow up paper. In order to simulate a battery environment

upon operation, an ultra-high vacuum (UHV)-compatible coin cell configuration was employed to study in *operando* for the first time the behavior of an anatase-TiO_2 electrode upon cycling. The results herein reported evidence the structural changes of the anatase TiO_2 anode upon sodium insertion, both in terms of oxidation and coordination state of Ti, unveiling the amount of reversible and irreversible sodium uptake per formula unit of TiO_2.

2. Experimental Section

2.1. Electrode Preparation, Cell Assembling and Electrochemical Characterization

Electrodes were prepared by doctor blade casting a slurry prepared by dispersing 80 wt% active material, *i.e.* anatase TiO_2 nanoparticles (synthesized as described elsewhere[16] with a 15 nm average diameter), 10 wt% PVdF binder (Solef 5130) and 10 wt% conductive agent (SuperC65, IMERYS, Switzerland) in N-methyl-2-pyrrolidone (NMP) on a 6 μm Al foil (Sigma-Aldrich) as current collector. After drying at 60 °C overnight in an oven (Binder), 12 mm diameter electrodes were punched and dried again overnight at 120 °C under vacuum.

The electrochemical tests for the *operando* XANES measurements were performed using an in-house modified standard CR2032 coin cell (see Section 4.4). The electrochemical cell was assembled inside an argon-filled glove box with H_2O and O_2 contents < 1 ppm, by using Na metal (99.8 %, ACROS ORGANICS) as counter electrode and a glass fiber (GF/D, Whatman) as the separator soaked with 1 M solution of $NaClO_4$ (98 % Sigma-Aldrich) in a mixture of ethylene carbonate (EC, UBE) and propylene carbonate (PC, Sigma-Aldrich) (1:1 v/v).

The cell was galvanostatically charged and discharged within the 0.02 - 2.00 V voltage range using a SP-200 Potentiostat (BioLogic). A constant current of 0.027 mA·cm^{-2} was applied during the first two cycles, and a potentiostatic step of one hour was added at the end of every charge

and discharge process. For the following cycles, increasing current values were applied, i.e. 0.106 mA·cm^{-2} for the 3rd cycle and 0.707 mA·cm^{-2} for the 4th and 5th cycle) with shorter potentiostatic steps at the end of charge and discharge (15, 5, and 25 min for the 3rd, 4th, and 5th cycle, respectively). During the fourth cycle, XANES measurements were not recorded.

2.2. Reference Compounds Characterization

The 270 nm thick amorphous TiO_2 reference sample was obtained by Radio Frequency (RF) sputtering a TiO_2 target (99.9 %, LESKER) at 100 W and 274 V in Ar atmosphere on a Si substrate. The structural properties of the thin film were investigated by XRD analysis under Ar atmosphere by using an air-tight sample holder. The diffraction pattern (see **Figure S18**) was collected in the SCALA laboratory which is part of the EMIL infrastructure on a Bruker D8 diffractometer using Cu K$_\alpha$ radiation ($\lambda_{Cu-K\alpha}$ = 1.54187 Å) in grazing-incidence geometry over a 2θ range of 20-100°. A step size of 0.02° and a 3° incident angle was used, along with a 2.5° primary Soller slit to define the beam.

11 nm and 40 nm carbon coated anatase TiO_2 reference samples were synthesized using anchoring block copolymers with hydroxamate as coordinating species, followed by a thermal annealing step.[16] The carbon coated Ti_4O_7 mesoporous powder was synthesized using porous poly(styrene-b-2-vinylpyridine) as templating agent as described elsewhere.[40]

The other reference samples (Ti metal foil, TiO, Ti_2O_3, and 15 nm TiO_2 powder) were purchased from Sigma Aldrich.

2.3. Operando X-Ray Spectroscopy:

The XANES measurements were performed in fluorescence mode in UHV (base pressure < 1×10^{-8} mbar) to increase the collected photons' attenuation length at the HiKE endstation[41] located at the BESSY II KMC-1 beamline[42] (beam focus size 0.1 x 0.1 mm^2)[43] at HZB, using a Si (311) crystal monochromator (energy resolution of 0.5 eV at 5000 eV) and a Bruker XFlash 4010 fluorescence SDD at 10°.[42] The measurements have been performed in vacuum, since the measurement setup is shared with photoelectron spectroscopic methods that require higher vacuum. In fact, we have used these capabilities to study the chemical composition of the SEI on TiO_2 electrodes and will publish these results soon. The photon energy scale was calibrated according to the endstation standard procedure, measuring the Au $4f_{7/2}$ core level of a clean gold foil by hard X-ray photoelectron spectroscopy at excitation energies of 4920 and 5060 eV (i.e. at the start and end energy of the XANES scan) before and after the *operando* experiment and putting its binding energy at 84.00 eV. No drifts or shifts of the photon energy were observed during the experiment.

All spectra were measured with the same experimental resolution, allowing direct comparison among the pre-edge peak intensities. Since the investigated electrode contains randomly oriented anatase TiO_2 nanoparticles, the sensitivity of XANES towards orientation can be neglected. The Ti K-edge spectra were normalized by the current measured at the ionization chamber situated after the last beamline aperture right before the analysis chamber and a linear function was subtracted from the result to remove the absorption threshold region. In order to get comparable results, the spectra were normalized by the intensity averaged between 5055 and 5060 eV. The data points around the narrow intensity dips observed at 4976 eV and 4991 eV arising from the crystal monochromator glitches were removed before the data evaluation.[44] Each spectrum was collected during 20 min and in total 108 spectra were measured. During the first sodiation

(discharge) process 36 spectra were recorded, further details are presented in the supplementary information S.I. Section 7, in Table S1.

2.4. Coin Cell Adaptation

Figure 1 (a) shows a schematic of the electrochemical cell set-up employed for the *operando* XANES measurements. A CR2032 coin cell was adapted to enable the spectroscopic investigation while being UHV-compatible. For this purpose, the coin cell lid was equipped with a 3 mm hole covered with a piece of 30 μm thin Kapton® foil (attenuation length of around 275 μm at 5000 eV)[45] using a two component epoxy glue (UHU sofortfest).

The hole size is a crucial parameter, since it has to be large enough to allow photons in and out during the measurements, but at the same time be small enough to guarantee a good electrical contact between the current collector and the coin cell lid around the hole covered by isolating Kapton® foil. The photon transmission (in and out) through the Kapton foil window and aluminum foil current collector is around 37 %, assuming incoming photons with an energy of 5000 eV and outgoing photons with an energy of 4500 eV.

The adapted coin cell was then mounted on an in house-modified sample holder with 13 electrical contacts (SHOMEC13) from FERROVAC GMBH. The pins ensure electrical contact with the sample stage once the holder is completely inserted. The system was connected over an electrical feedthrough with a Potentiostat SP-200 (Biologic) enabling electrochemical tests in UHV conditions.
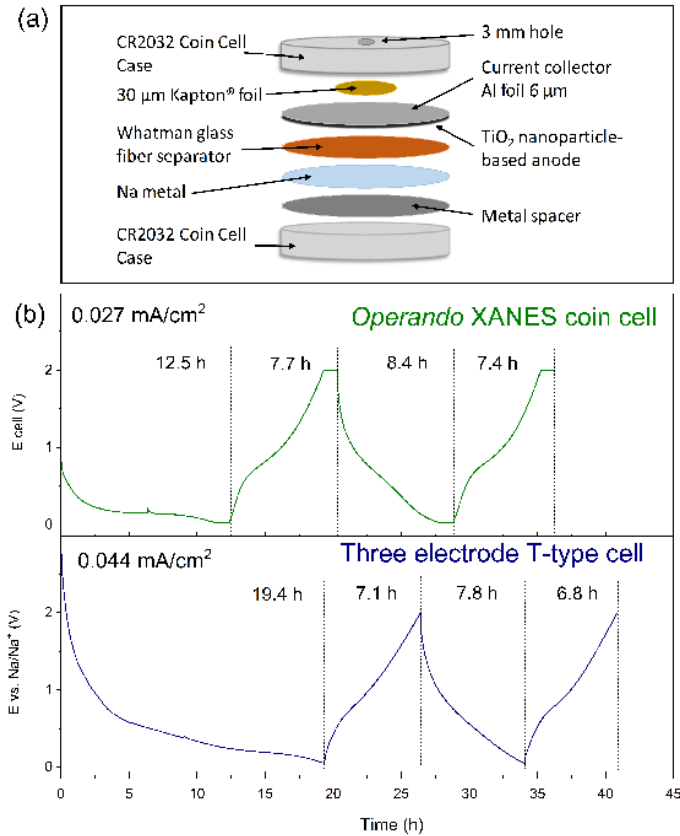
Figure 1. (a) Scheme of the coin cell setup used for the operando XANES measurements. The hole in the coin cell lid enables photons moving in and out. The UHV-window consists of a piece of 30 μm thin Kapton® foil whilst the current collector is a 6 μm thin Al foil. (b) Comparison of the voltage profile obtained with the adapted coin cell (green curve) and a standard three electrode T-type Swagelok® cell.

Figure 1 (b) shows the comparison between the voltage profiles obtained by cycling the TiO_2 based electrode in the adapted *operando* XANES coin cell and a standard three electrode T-type cell. Despite the slightly different applied current and the difference in the time required for the first sodiation process (most likely related to the different open circuit voltage (OCV) of the two

cells), the voltage signature is overall quite comparable, suggesting a good agreement of the electrochemical features related to the structural changes between the two cell configurations.

2.5. Data Evaluation

The Ti K-edge of anatase TiO_2 exhibit a characteristic 4-feature pre-edge structure.[46–51] Usually, a qualitative approach to analytically process the Ti K-edge spectral features consists in modelling the pre-edge region with a combination of four peak-functions (Gaussian, Lorentzian and Voigt), which generally allows comparing values of different experiments reliably.[46–51] In this study, the pre-edge regions of the collected *operando* spectra were fitted using an arc-tangent function and four Gaussian functions (sorted by increasing absorption energy, E_{exc}) as described by equation (1) reported below.

$$I(E_{exc}) = I_0 + A_t \, arctan\left(\frac{E_{exc}-E_t}{w_t}\right) + \sum_{i=1}^{3} \, A_i \left(e^{-\frac{(E_{exc}-E_i)^2}{2\,w_i^2}} \right) + B \left(e^{-\frac{(E_{exc}-E_B)^2}{2\,w_B^2}} \right) \quad (1)$$

The analytical fitting procedure gives comparable values with respect to literature for the pre-edge positions (E_1, E_2, E_3 and E_B, as shown in Figure S3), full width at half maximum (FWHM), and intensities (A_1, A_2, A_3 and B see Figure S3), as well as the absorption edge position (E_t). The FWHM of the A_1, A_2 and A_3 peaks is kept equal for each spectrum ($w_1 = w_2 = w_3$) but can differ from the B peak (w_B). The arc-tangent function used to simulate the absorption edge jump[46,52] involves the offset (I_0) and consists of an amplitude A_t and a parameter describing the width w_t. The same fitting procedure was also used for the spectra of the reference materials, though the number of Gaussian functions was adjusted for each material to minimize the least square function, especially for oxides with a lower valence number. The results of the analytical fit were used to obtain the maximum intensity and position of the pre-edge region.

Another approach used to analyze XANES spectra is the principal component analysis (PCA),[53] which allows the imposition of different chemical species to the measured spectrum and the identification of likely present species thus involving the comparison of the obtained spectra with those observed for reference materials. PCA is a powerful tool when analyzing a large data set, allowing decomposing the raw data into singular relevant information and revealing possible contributions from different chemical species in the observed spectra. Indeed, each measured spectra can be simulated by using a linear combination analysis (LCA) of selected reference materials. This approach is physically more meaningful and considers the whole spectra rather than only the pre-edge region as in the previous method. On the other hand, it is a time-consuming process relying on the identification and spectra measurement of reliable and chemically stable reference materials. In this work, this second approach is used, assuming the sample is composed of oxide components to quantitatively[54,55] analyze the XANES data. The PCA and target transformation study was performed using the SixPACK software in which the spectra (corrected as described in Section 2.3) were input independently.[56] While implementing the PCA analysis, the *operando* spectra were fitted by using a linear combination of the spectra of four reference materials. The fit was optimized by a least-squares minimization, with a trust region reflective method. The *operando* spectra, sorted chronologically, were fitted consecutively, using the previous linear combination parameters as the new initial parametric set. The goodness of the fit was calculated by normalization of the least square sum of each spectra to the poorest obtained fit (0 %) and the best possible fit (100 %) defined by a zero least square sum. A value for the oxidation state of Ti was extracted from each spectrum by weighing the nominal oxidation state of the four reference materials with their spectroscopic contribution to the fit obtained with the linear combination.

Based on the oxidation state derived from the spectra, the total amount of sodium per formula unit of TiO_2 inserted during the first sodiation step was calculated by subtracting the oxidation state of the measured pristine spectrum from the oxidation state of the measured sodiated spectrum at the end of the 1st discharging step. The number of Na ions irreversibly trapped in the TiO_2-based anode per formula unit of TiO_2 was derived by the difference of the valence state of the original pristine spectrum and that of the anode in a fully charged state. The difference between the total and irreversible inserted sodium is the number of reversibly inserted sodium ions per formula unit of TiO_2. For the following cycles the amount of sodium per formula unit of TiO_2 inserted reversibly is calculated from the difference between the Ti oxidation state at the beginning and the end of each cycle, while the irreversible amount of sodium is derived from the comparison of the last spectrum of the charging step with the last spectrum of the previous charging step. The uncertainty in the linear combination fit of each spectrum was used as a measure of the uncertainty in the determination of the oxidation state and in the amount of inserted sodium. The values for the oxidation state of the fully sodiated and fully desodiated state were averaged over up to three spectra, if possible. Hence, the uncertainties are much larger for the later cycles due to the reduced number of measured spectra compared to the first two cycles, which were (dis-)charged at lower currents.

In the last Section of this work, our data are compared with literature.[34,38,39] The energy alignment between the measurements presented in this paper and those of Farges et al.[34] is based on the position of the Ti metal pre-edge peaks.

3. Results and discussion

Figure 2 displays the evolution of the Ti K-edge spectra collected upon cycling of the anatase TiO_2 electrode using the in-house designed coin cell described in the Experimental section. The contour plot shows the measured *operando* spectra alongside the corresponding voltage profile. Selected spectra measured at relevant (dis-)charging states are highlighted in the contour plot and reported in the bottom panel of Figure 2.

The XANES Ti K-edge spectrum originates from transitions from the Ti 1s core-hole state into the empty states above the Fermi level corresponding to (hybridized) O 2p, Ti 4s, Ti 4p and Ti 3d derived orbitals. For our discussion, we divide the XANES spectra into three main regions, namely the pre-edge region (until around 4975 eV), the post-edge region (starting at around 4985 eV; described further in the S.I. Section 1 and **Figure S1**) and the absorption edge in between these regions. The Ti K spectra for the pristine and cycled TiO_2 electrodes are shown in the bottom panel of Figure 2 and four characteristic pre-edge features referred to as A_1, A_2, A_3, and B are presented. In **Figure S2** (see S.I. Section 2), the Ti K pre-edge features of three anatase TiO_2 reference samples are reported for comparison.
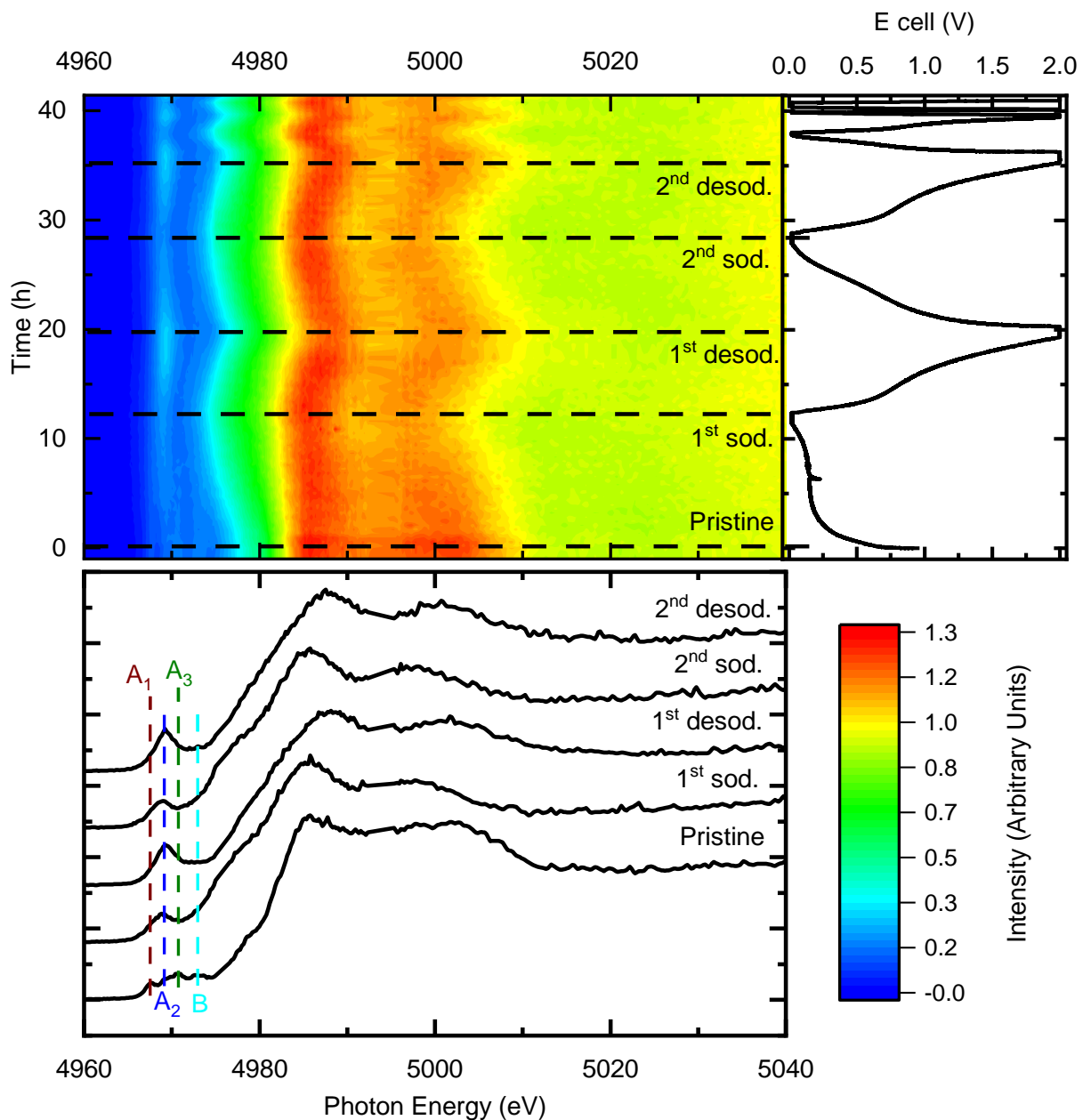
Figure 2. *Operando* XANES measurements of a TiO$_2$-based anode for SIBs. The color contour plot in the top left panel shows the changes in the XANES Ti K-edge over time. The top right panel depicts the potential profile as a function of time. The bottom panel shows characteristic spectra at relevant (dis-)charging states indicated by horizontal dashed lines in the contour plot.

A_1, A_2, and A_3 peaks are assigned to transitions from Ti 1s to Ti 3d-4p hybridized states,[46–48,57] with the A_2 component generally not observed in the rutile structure.[58] Feature B can be assigned to transitions from Ti 1s to Ti 3d (e_g)-4p hybridized states[46,47] but has also been attributed to Ti 1s to Ti 4p-4s transitions and/or O 2p hybridized states having mainly a Ti 4p character.[34,48,57,59] The 1s to 3d transition is dipole forbidden if no p-d mixing occurs, thus the pre-edge intensity can be considered as a direct measure of the p-d-mixing (quadrupole effects excluded) arising from the deviation of the 6-coordinated centrosymmetric octahedral structure around the Ti atom.[23,29,31,34,38] The Ti atoms in anatase TiO_2 have a 6-coordinated local D_{2d} symmetry, which is a slightly distorted octahedral symmetry with two oxygen atoms on one axis having a larger distance from the central Ti atom compared to the other four oxygen atoms on the same plane.

The anatase features begin to smear out soon upon sodiation. At 0.02 V, i.e. at the end of the first sodiation process, the characteristic four-peak feature of the anatase structure in the pre-edge region disappears, as shown in Figure 2. Specifically, the intensity of the A_3 and B peaks decreases, while the A_2 peak intensity increases. During the following desodiation, the intensity of the pre-edge peak A_2 increases further, irreversibly deviating from the spectral shape of the pristine electrode. The intensity changes in the pre-edge occur cyclically upon (de-)sodiation. In addition, a change in the position of the absorption edge is also observed, with a shift towards lower excitation energies during sodiation and towards higher energies upon desodiation (see also contour plot in Figure 2).

Although some features tend to regain the shape and position observed in the pristine spectra upon desodiation, the original anatase spectrum is never completely recovered, as reported previously by Greco et al. on *ex-situ* carbon coated TiO_2 samples in different cycling stages.[23]

This is the case especially in the pre-edge region, suggesting that irreversible structural changes of the electrode material arise during the first sodiation, while the subsequent structural rearrangements are reversibly occurring upon following cycles.

A large set of information related to the valence and coordination state of Ti in the electrode can be derived from the correlations between intensity of the pre-edge peaks and the main-edge position. Therefore, the set of *operando* spectra was fitted according to the first approach described in the Experimental section, *i.e.,* using a combination of four Gaussian functions and one arc-tangent function.[46,48,49,51,52] revealing the variation of the oxidation state of Ti upon cycling as described in detail in the S.I. Section 3, which provides additional information about the application and interpretation of the different parameters of the analytical fit. For instance, two examples of the pre-edge fit are shown in **Figure S3** and the absorption edge position plotted against the nominal oxidation number of measured reference materials is displayed in **Figure S4**.
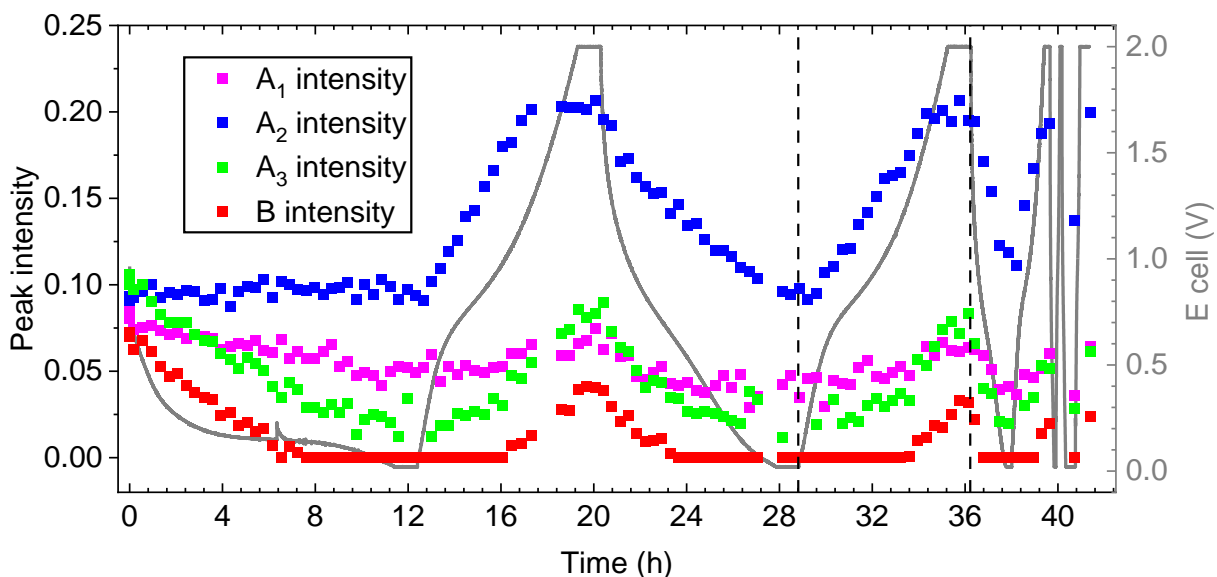
Figure 3. Evolution of the intensity of the 4 peaks fitted at pre-edge region during (dis-)charging of the coin cell. In gray the voltage profile of the first 5 cycles.

The results obtained using this analytical fitting approach are displayed in **Figure 3**, reporting the calculated intensities of the four pre-edge peaks alongside with the measured voltage profile over time (gray-line). Upon desodiation a decrease of the Ti coordination state is observed as indicated by the increase of the pre-edge peak A_2,[23,29,32,34,38] suggesting that the original pristine structure is not recovered as a consequence of an irreversible atomic structural change of the anatase TiO_2. This result is in good agreement with other previously reported studies.[8,11,22–25] Other influences at the pre-edge peak intensity and position (shown in **Figure S5**) are discussed in the S.I. Section 3, though they can be largely neglected in comparison with the large effects arising from coordination and oxidation state variation, which influence the absorption edge and pre-edge region of the spectra.[29,34,38,39]

In order to separate the two effects, i.e., oxidation and coordination variations, and obtain further details on their variations, a second data evaluation method was conducted, a linear combination analysis LCA, by using reference spectra of selected Ti-based oxide materials chosen by the results of the principal component analysis (PCA)[53] and target transformation methods detailed in the Experimental section.

The results of the PCA and target transformation suggest that four different species are present in the *operando* data (see **Figure S6**). Indeed, by using a 4-component target transformation, results indicate no presence of metallic Ti, TiO, and Ti_2O_3 (shown in **Figure S7-S9**), while the spectra of the Ti_4O_7 reference, anatase TiO_2 powder, amorphous TiO_2 thin film, and carbon coated anatase TiO_2 powders could be reproduced (see **Figure S10-S14**) and, therefore, are the most probable compounds appearing in the *operando* experiment. It has to be stated, that the

good reproducibility of these species is not a prove for their formation, nevertheless the formation of species with similar properties, i.e., degree of crystallization, Ti coordination, stoichiometry and Ti oxidation state is likely, since these effects influence the XANES spectra the most. On the other hand, the target transformation allows to exclude the formation of species and in this case no evidence of Ti metal (or TiO) formation during the sodiation process was found, suggesting that the sodium uptake on the TiO_2 structure is based solely on the insertion of the Na^+ ion within the oxide structure, in contrast to other reaction mechanisms proposed elsewhere.[8,25,60,61] Moreover, the presence of Ti_4O_7 in the target transformation analysis hints at the appearance of oxygen loss during the (dis-)charging, which will be discussed in more detail regarding the LCA results.

Based on the PCA results, which are described in detail in the S.I. Section 4, and the good reproducibility of the target transformation, Ti_4O_7, amorphous TiO_2, and anatase 15 nm TiO_2 powder were the reference spectra chosen for the LCA approach (the fits are displayed in Figure S10-S12). Despite its lower target transformation reproducibility shown in Figure S9, the Ti_2O_3 spectrum was also used for the LCA due to the lack of a better Ti^{+3} reference. The results of the LCA applied to the complete *operando* XANES data set are shown in **Figure 4**, exhibiting the contribution of each reference component to the linear combination fit of the *operando* spectra upon cycling. Two examples for the LCA fit are presented in **Figure S15** in the S.I. in Section 5.
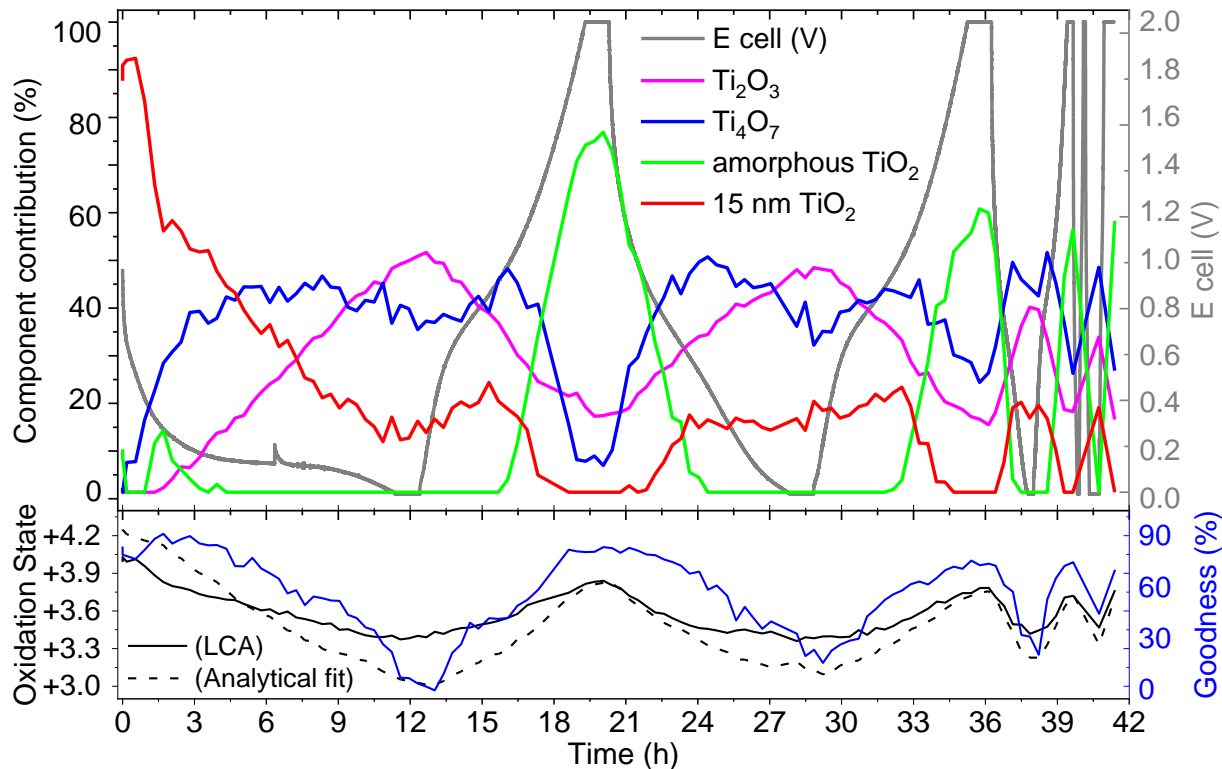
Figure 4. (Top panel) Evolution of the reference materials contributions (in percentage) to the *operando* spectroscopy data. The voltage profile upon time of the electrochemical cell is shown in gray. The uncertainty of the fit is around 10 %. (Bottom panel) Goodness of the fit in percentage of its maximum (blue curve) and the oxidation state of Ti derived from the LCA (black solid curve) and from the analytical fit (black dashed curve) upon cycling. The goodness of the fit is normalized so that 100 % correspond to the best possible fit achievable and 0 % to the worst fit obtained. More details towards the goodness of the fit can be found in **Figure S16**.

Upon sodiation, the contribution to the overall fit of the 15 nm TiO_2 anatase reference decreases from around 100 % in the pristine material to values below 20 % at the end of the sodiation process (0.02 V). Simultaneously, the Ti_2O_3 contribution (Ti^{+3}) increases, indicating that TiO_2 (Ti^{+4}) is reduced due to Na^+ uptake. The contribution of the Ti_4O_7 phase ($Ti^{+3.5}$) rapidly

increases at the beginning of the sodiation and stabilizes at values between 40 % and 50 % thereafter. The increased Ti_2O_3 (Ti^{3+}) contribution corresponds directly with a decrease in the goodness of the fit, presented in the bottom panel of Figure 4. This is associated with the absence of a good (stable) reference compound for Ti in the 3+ oxidation state, as discussed extensively in the S.I. Section 5. A detailed view at the goodness of the fit is offered by the contour plot reported in Figure S16 showing the squared residual divided by the intensity for all the LCA fits.

During the following desodiation, the contribution of anatase TiO_2, Ti_2O_3, and Ti_4O_7 decreases, while the amorphous TiO_2 component strongly increases, indicating for a nearly completely (80 %) amorphous structure of the active material and the complete disappearance of the anatase crystal structure in the desodiated state (spectra at 2.0 V). The remaining 20 % of the signal arises from a marginal mixture of species with a lower oxidation number, *i.e.* Ti_2O_3 and Ti_4O_7.

The original TiO_2 anatase phase has thus evolved towards an almost fully amorphous structure with absence of long-range ordering. The residual consists of the species with a valence lower than +4, *i.e.*, Ti_2O_3 and Ti_4O_7, which are most likely associated to the irreversibly trapped sodium ions in the structure, responsible for the first irreversible capacity observed in the voltage profile. It is worth mentioning that since the Ti K-edge spectra of the desodiated electrode only needs a small contribution of Ti_2O_3, thus the goodness of the fit reaches its best values in comparison to the low fit quality observed in the fully sodiated states. The trend observed during the first sodiation and desodiation processes is also confirmed during the following cycles.

Based on the interpretation of the reported LCA results, the proposed $Ti^{4+/3+}$ redox activity well matches the voltage profile features observed at ~0.8 V in discharge and ~1.0 V in charge, characterized by a slight change of the curvature of the voltage profile (see Figure 4 top panel, gray curve) as already observed in similar electrode materials.[16] Indeed, Figure 4 shows that the

contributions arising from TiO_2-based references and Ti_2O_3 exchange their values in proximity of the curvature change in the voltage profile. This effect is observed during the first desodiation process but also in the subsequent cycles.

Although the contribution of the amorphous TiO_2 reference to Ti K-edge spectra of the sodiated TiO_2 anode (0.02 V) is mainly insignificant, amorphization of the active material during the first sodiation, i.e. loss of crystallinity, as previously reported,[8,23] cannot be excluded. Indeed, a temporary increase of the amorphous contribution is observed after approximately 1 h of cycling (see voltage profile at about 0.3 V) until about 3 h of cycling, after which the contribution decreases considerably and becomes negligible. This temporary increase of the amorphous contribution during the first sodiation process can be associated to the initial stage of the reported loss of long range ordering of the electrode and the formation of an unknown sodiated Ti^{3+} state reproduced by the Ti_2O_3 reference with the LCA procedure. Given the absence of a reference compound and its spectrum, the fit struggles to provide detailed information about the degree of crystallinity and coordination state of the highly sodiated electrode. In fact, the contribution of the anatase TiO_2 structure to the fit at highly sodiated states (almost 20 %) may be overestimated, as a recovery of long-range crystal ordering appears rather improbable especially for the sodiated state. Furthermore, it can be derived from the LCA results that 5-7 % of oxygen is removed from the electrode during the first 3 h of sodiation, which can be associated to the aforementioned amorphization and structural rearrangement undergone by the anode structure. These findings can be related to gas chromatography measurements of an anatase TiO_2 nanoparticle-based anode, where a large evolution of oxygen is observed during the first discharge of the battery.[8] In addition, LCA results (see **Figure S17**) of the pre-edge region, which is highly sensitive to the coordination and geometry of Ti, show an even higher

contribution of the amorphous reference sample during the first 7 h of discharge, down to 0.14 V, which further suggest an amorphization process during the first sodiation. Thus, amorphization of the electrode during the first sodiation, as observed in other studies,[8,11,23,24] is likely but cannot be proven by our measurement results.

As described in the Experimental section, the fit results were used to calculate the oxidation state of Ti for each spectrum, which is presented in the bottom panel of Figure 4 and compared with the values calculated with the analytical fitting approach. While the oxidation state of the desodiated electrode is in good agreement for both methods, there is a larger discrepancy for the sodiated state, albeit within the uncertainty range. The analytical fitting method shows that the sodiation of the electrode material causes a reduction of the oxidation state of Ti from $+4.2 \pm 0.4$ to $+3.0 \pm 0.3$. Upon desodiation, the oxidation state increases again to about $+3.8 \pm 0.3$, thus not recovering its original pristine value.

The LCA has been used to calculate the oxidation of Ti and the amount of sodium inserted by formula unit of TiO_2, as reported in **Table 1.** Therefore, an oxidation number of 4.00 ± 0.08 was used for the pristine Ti oxidation state as derived by the LCA fit. It is worth noting that despite there being an increased uncertainty on the percentage contribution of each reference species in the sodiated state, the accuracy on the calculation of the oxidation state can be justified by the improved goodness of the fit in the absorption edge region, which is the most sensitive part of the spectra in terms of valence state. Indeed, even in the fully sodiated state, where the use of the Ti_2O_3 reference limits its applicability, the position of the absorption edge is accurately reproduced (see Figure S16), indicating that the oxidation states can be calculated with a relatively small associated measurement uncertainty.

Table 1. Amount of inserted sodium per cycle[1]

	1st cycle	2nd cycle	3rd cycle	5th cycle
Current density (mA/cm^2)	0.027	0.027	0.106	0.707
Coulombic efficiency in %	60.0	82.4	88.8	100
Areal discharge capacity (mAh/cm^2)	0.32	0.22	0.18	0.16
Areal charge capacity (mAh/cm^2)	0.19	0.18	0.16	0.16
Oxidation number sod.	+3.39 ± 0.13	+3.38 ± 0.12	+3.42 ± 0.22	+3.47 ± 0.20
Oxidation number desod.	+3.82 ± 0.06	+3.76 ± 0.07	+3.72 ± 0.13	+3.77 ± 0.15
Na+ per formula unit	0.61 ± 0.13	0.44 ± 0.12	0.34 ± 0.22	*
Irreversible Na$^+$	0.18 ± 0.05	0.06 ± 0.07	0.04 ± 0.13	*
Reversible Na$^+$	0.43 ± 0.14	0.38 ± 0.14	0.30 ± 0.26	0.30 ± 0.25
Reversible Na$^+$ / total Na$^+$ in %	70.5	86.4	88.2	*

During the first cycle, around 0.43 Na$^+$ ions are inserted reversibly per formula unit of TiO$_2$ into the electrode material, and 0.18 Na$^+$ ions are trapped irreversibly in the first sodiation process. The reversible amount of inserted Na$^+$ ions slowly decreases until the third cycle, as well as the irreversibly inserted Na$^+$ ions. All the values are reported with an associated error (uncertainty range) and the observed changes are always within the uncertainty range.

The amount of Na$^+$ inserted reversibly changes only slightly in the first and second cycle, while for the third cycle, the lower value (0.30 ± 0.26) might be associated to the 4 times higher current density applied (0.106 mA cm^{-2} vs. 0.027 mA cm^{-2}) or to the increased number of cycles.

---

[1] **Table 1.** LCA derived oxidation state of Ti in the fully sodiated or desodiated state during the 1st, 2nd, 3rd and 5th cycles. Associated calculated values of irreversible and reversible inserted sodium atoms per formula unit of TiO$_2$ are reported together with the areal charge and discharge capacity and the Coulombic efficiency calculated for each cycle by dividing the charge derived during discharge by the charge applied during the charging process of each cycle. *Cannot be calculated without the value of the 4th cycle.

Regarding the irreversibly inserted Na$^+$ ions, the first cycle presents the highest value of trapped sodium (0.18 ± 0.05). This is likely related to the large structural transformations of the nanoparticles during the initial discharging process and can be partially attributed to the sodium trapped in the newly formed amorphous structure. Additionally, some sodium contributes to the formation of the SEI. Indeed, a neat decrease of the trapped Na$^+$ to (0.06 ± 0.07) for the second cycle and (0.04 ± 0.13) for the third cycle is observed, associated to an improved reversibility of the overall (de-)sodiation process upon cycling as demonstrated by the increasing Coulombic efficiency values, typically observed for improved SEI passivating properties upon cycling. In fact, the ratio of reversible to total inserted Na$^+$ is in a good agreement with the Coulombic efficiency, which suggests that the majority of the irreversible inserted sodium ions is trapped during the large structural rearrangements occurring in the first (and to some extend also in the following) cycle(s) . This might hint at an incomplete sodiation of the anode during the first cycle maybe caused by the *operando* coin cell setup. Until the third cycle, the Coulombic efficiency and the ratio of the inserted sodium ions are converging, which suggests that the amount of sodium lost in side reactions like the SEI layer formation is constantly decreasing with an increasing number of charging cycles.

Overall, the Na$^+$ ions cycled reversibly and irreversibly during the first cycle are in good agreement, within the uncertainty range, with the values calculated by Wu et al.,[8] reporting on 0.28 Na$^+$ ions per formula unit irreversibly trapped and around 0.41 Na$^+$ ions reversibly inserted. Furthermore, the Coulombic efficiency shows good conformity with the ratio between total and reversible inserted sodium.

It is worth noting that by means of the linear combination fit of the selected reference materials (LCA), the oxidation state and, thereby, the amount of reversible and irreversible Na$^+$ ions

inserted per formula unit of TiO_2 is determined with higher precision compared to the values obtained by using the analytical fit. Indeed, while for the LCA the complete energy range of the spectroscopic data set is used, for the analytical fit approach only the pre-edge region is considered, as discussed in the S.I. Section 5. Additionally, the oxidation numbers obtained by the LCA are less affected by changes of the coordination state or the crystallinity of the electrode and thus better disentangle the different influences on the spectrum.

A change of the coordination state as suggested by the analytical fit during the electrode's desodiation cannot be confirmed nor excluded by the LCA due to the unknown coordination state of the amorphous TiO_2 reference sample.

Previously reported molecular dynamic and reverse Monte Carlo simulations indicate that amorphous TiO_2 nanoparticles present a distorted octahedral configuration with six oxygen neighbors in the bulk,[62,63] and 5-coordinated Ti atoms dominating the surface structure characterized by oxygen vacancies. It is proposed that the relative influence of the surface oxygen vacancies on the overall coordination state should be limited as long as the particles size exceeds a few nanometers.[63,64]

A clear identification of the coordination states of Ti in the amorphous reference sample and in the fully sodiated electrode state, despite the complementary results obtained by the LCA and analytical fit approaches, still remains an open question.

Nonetheless, further analysis of the pre-edge fit exploiting the pre-edge position and intensity could shine some light on the question. The pre-edge region is very sensitive to valence and Ti coordination; indeed, several studies have demonstrated a direct relationship between these properties and the spectral features observed in this region.[29,34,38,39] Therefore, in the following

we compare the results obtained from the analytical pre-edge fit with previously reported studies,[29,38,39] especially focusing on the results of Farges et al.[34]

Figure 5 shows the relation between the pre-edge peak maxima intensities and positions of the *operando* Ti K-edge XANES spectra obtained in this work in comparison with the values obtained for the measured reference compounds (in magenta) and literature values obtained by Farges et al. (black triangles).[34] The pre-edge maxima of the reference spectra are shown as magenta open circles, and the *operando* data are shown as solid squares, color-coded according to the potential of the cell. The different Ti^{+4} reference materials with 4-, 5- and 6-coordinated structures measured by Farges et al.[34] are grouped in three separate (gray) blocks, while values calculated for mixed Ti^{+4} species with different coordination states lie outside of the gray areas. The coordination of Ti is indicated within the squared brackets. While a comprehensive description of the interpretation of Figure 5 can be found in the S.I. Section 6, here the main outcomes are discussed.

From the position and peak intensity of the investigated reference spectra, it can be derived that all reference samples are in a 6-coordinated state, except for the expectedly 6-coordinated[62,64] amorphous TiO_2 reference, which shows a non-negligible amount of 5-coordinated titanium. This result matches with the findings reported in this work, since the analytical fit revealed a 5-coordinated phase, and the LCA suggested a mainly amorphous phase for the desodiated state, and in previous work.[23] For the *operando* spectra reported in this work, Figure 5 clearly shows a shift of the position of the pre-edge maximum (related to the reduction of the Ti atoms on the electrode) towards lower energy values and a slight increase of the intensity during the first sodiation. Upon desodiation, the intensity increases significantly, and the maximum position shifts back to higher energies. As discussed in the S.I. Section 6, this

trend indicates that a non-negligible amount of the 6-coordinated Ti transforms into a 5-coordinated structure along the desodiation process in agreement with previously reported results by Greco et al.[23] This observation is further supported by the LCA results, where the large contribution of amorphous TiO_2 at the fully desodiated states can be attributed to the reduced coordination of this reference.
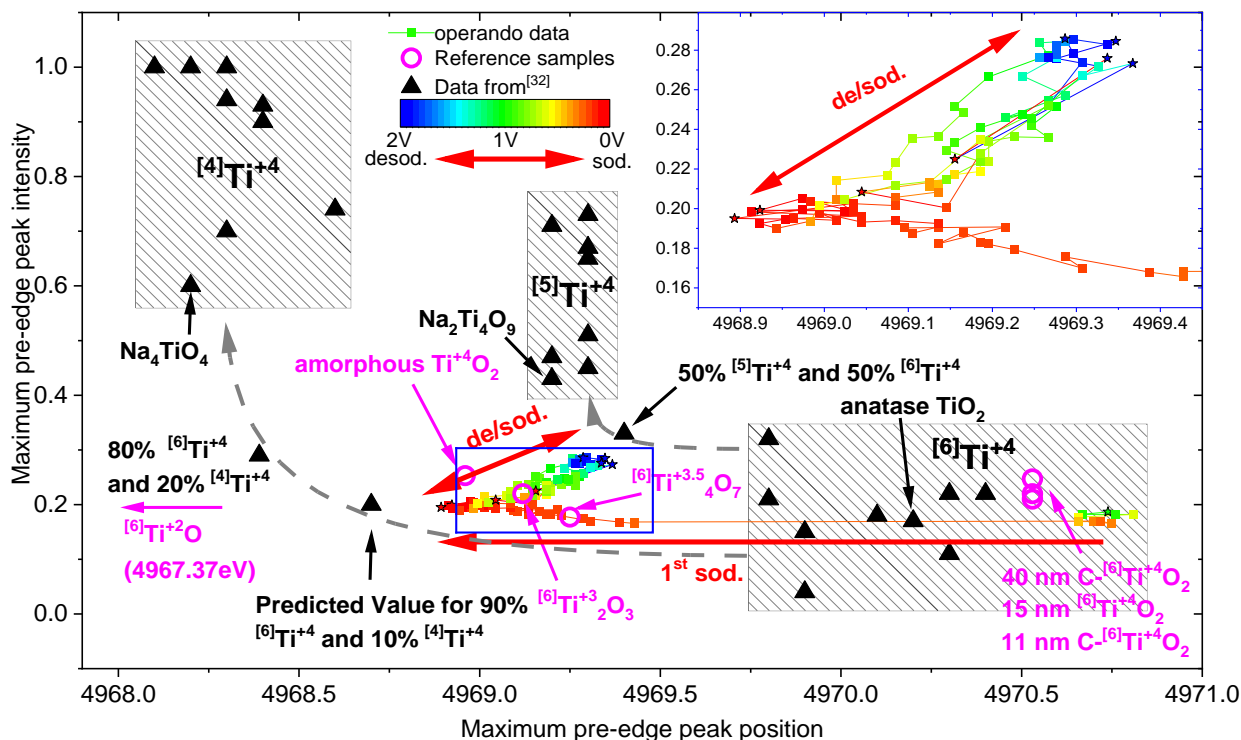
Figure 5. Relation between pre-edge peak maxima intensities and positions of the *operando* Ti K-edge XANES data, in comparison with the values obtained from the measured reference compounds (in magenta) and literature values obtained by Farges et al.[34] (in black). The color code of the operando data set indicates the average voltage of the cell in which the spectrum was recorded from 0 V (red) to 2 V (blue). The pristine and fully (de-)sodiated spectra are indicated with stars. The average uncertainty for the pre-edge peak maximum position is 0.1 eV. The inset in the upper right corner is a magnified view on the operando data. The gray blocks include

different Ti^{+4} reference materials with 4-, 5- and 6-coordinated structures measured by Farges et al. The coordination of Ti is indicated within the squared brackets.

The exact coordination of the sodiated state remains unclear, due to the spectral convolution arising from the changes in oxidation and coordination state. However, it can be inferred by comparing the *operando* data with the simulated 4 and 6 coordinated Ti^{+4} species in Figure 5[34] that a 4-coordinated titanium can be excluded to an amount below 10 %, in agreement with Greco et al.[23] A precise quantification of the coordination state requires density functional theory (DFT) calculations, which are planned for a future work.

In the results reported in this work, it is observed that upon further sodiation of the electrode a change of the pre-edge structure compared to the spectrum of the first fully desodiated state occurs. Whether this change is solely related to the change in the Ti valence state or also includes a potential recovery of the 6-coordinated original structure cannot be unequivocally derived from the spectroscopic data, since the relation between pre-edge peak intensity and the coordination state for Ti^{+3} species has never been reported on literature. However, the formation of 5-coordinated Ti^{3+} sites at oxygen vacancies and/or Ti interstitials in anatase TiO_2 is extensively discussed in literature based on DFT calculations, and its existence cannot be excluded.[65,66]

Assuming that the distortion (lowering) of the 6-coordinated structure occurs already during the first sodiation, as suggested by the pre-edge peak changes and the oxygen loss observed during the first 3h, a plausible hypothesis is that the structural distortion might be associated to the amorphization and oxygen removal in the TiO_2 electrode, as reported in other studies.[8,11,23] The loss of the long-range order of the anatase structure and the increase of the grain boundary contributions enhance the role of interfaces between nanodomains, where more defect states and dangling bonds could be present, resulting in an increased amount of 5-coordinated Ti and

oxygen vacancies. The alternative, i.e. an initial lowering of the coordination state observed during the first desodiation is difficult to explain, since it is unlikely that the release of sodium, which is an energetically favored process compared to the sodiation, induces a coordination change in the Ti-centered structure.

Further insights into the nature of the species largely contributing to the fully sodiated state of the electrode can be obtained by comparing the spectroscopic data of sodium titanates compounds labeled in Figure 5. The high oxidation state (Ti^{4+}) of $Na_2Ti_4O_9$, Na_4TiO_4 (indicated in Figure 5), and other titanates, such as $Na_2Ti_3O_7$, Na_2TiO_3, $Na_4Ti_5O_{12}$ and $Na_{16}Ti_{10}O_{28}$, reported in literature[67,68] excludes them as matching candidates for the observed unknown sodiated phase. Sodium titanates with a lower oxidation number, such as $NaTi_2O_4$ or $NaTi_8O_{13}$, are very rarely reported and only in a crystalline phase.[69,70] Due to the lack of related XANES data reported, it cannot be totally excluded that the mentioned sodium titanate compounds present a similar stoichiometry to the unknown sodiated phase, but their crystallinity makes them unsuitable as reference samples for the sodiated titanate phase.

In summary, the Ti K-edge XANES *operando* data set was analyzed using two different approaches. The results of both evaluation methods have been compared and discussed with respect to the literature. The results on the oxidation state of Ti obtained by the LCA are more accurate than the analytical fit and in better agreement with the previously reported values for inserted Na^+ ions in an anatase TiO_2 structure.[8] The comparison of the *operando* Ti K-edge spectroscopy data with XANES literature[29,34,38,39] supports the results derived from the different evaluation approaches, suggesting that the 6-coordinated TiO_6 structure is indisputably changed (partially) into a 5-coordinated state during the first desodiation. Whether the coordination of the Ti atoms remains unchanged upon the first sodiation is still unclear, though might have been

triggered by the drastic reconfiguration of the electrode structure. An experimental demonstration of the coordination state of Ti in the sodiated state would require the identification of reference samples consisting of sodiated Ti complexes with lower coordination and oxidation numbers than the one presented by the pristine anatase TiO_2. In this regard, the comparison with the data reported by Farges et al.[32,34] revealed that the unknown sodiated Ti species consists most likely of a mix of 5- and/or 6-coordinated Ti species, excluding a possible 4-coordination.

4. Conclusions

In this work, for the first time an *operando* X-ray absorption near-edge structure spectroscopy experiment at the Ti K-edge has been performed on a TiO_2 anatase nanoparticles-based anode for SIBs. An in-house modified coin cell equipped with a UHV compatible window was used to collect the spectra at the Ti K-edge during the (de-)sodiation process of the electrode. The collected spectroscopic data give insights into the coordination and valence state of Ti and on the crystallinity of the anatase structure upon cycling. A detailed analysis of the *operando* XANES spectra suggests that around 0.43 Na^+ ions per formula unit of TiO_2 are inserted reversibly and 0.18 Na^+ ions are irreversibly trapped during the first cycle, in good agreement with previous works, explaining the low Coulombic efficiency of anatase TiO_2-based anodes during the first cycle. Furthermore, formation of appreciable amounts (within the detection limit of XANES) of metallic titanium (Ti^0) or Ti^{+2} during the sodiation process could not be observed. The analysis of the electrode in the desodiated state shows a distortion of the 6-coordinated symmetry towards a 5-coordinated TiO_5-structure (around 50 %) and an amorphization of the electrode structure most likely associated to the irreversible loss of oxygen during the first sodiation process, which further suggests that the amorphization and the decrease of the Ti coordination state already take

place during the first sodiation. A better understanding of the impact of the ligand strength on Ti^{3+} ions and its effect on the XANES spectrum is needed to reveal in more detail the suggested distortion of the 6-coordinated Ti structure during the first sodiation process, though a change into a 4-coordinated structure can be excluded. Therefore, MCR and DFT analysis are planned to reveal the structural changes during the first sodiation in more detail and will be presented in a future paper.

In addition, it is found that the original anatase structure of the TiO_2 nanoparticles is not recovered upon desodiation, as suggested by the disappearance of the spectral features in the pre-edge region of the Ti K-edge XANES spectrum of the pristine anatase TiO_2. The subsequent cycling of the TiO_2-based electrode leads to the same spectroscopic changes observed after the first sodiation, revealing a stable (and reversible) Na^+ insertion after the irreversible structural rearrangements of the TiO_2 nanoparticles observed during the first cycle.

The analysis of the Ti K-edge of an *operando* XANES experiments of an anatase TiO_2-based electrode provided in this work, contributes with a coherent and comprehensive picture to the highly debated mechanism governing the sodiation mechanism of TiO_2 anodes.

Supporting Information

The following files are available free of charge.

Supporting Information including a post edge feature discussion, fit examples, target transformation results, fit residuals and XRD measurements are given in

09_06_20_ACS_SI_Paper_Operando.docx

Corresponding Author

Andreas Siebert

Interface Design, Helmholtz-Zentrum Berlin für Materialien und Energie GmbH (HZB),

Albert-Einstein-Straße 15, 12489 Berlin Germany

andreas.siebert@helmholtz-berlin.de

References

(1)   Wadia, C.; Albertus, P.; Srinivasan, V. Resource Constraints on the Battery Energy Storage Potential for Grid and Transportation Applications. *Journal of Power Sources* **2011**, *196* (3), 1593–1598. https://doi.org/10.1016/j.jpowsour.2010.08.056.

(2)   Ponrouch, A.; Monti, D.; Boschin, A.; Steen, B.; Johansson, P.; Palacín, M. R. Non-Aqueous Electrolytes for Sodium-Ion Batteries. *Journal of Materials Chemistry A* **2015**, *3* (1), 22–42. https://doi.org/10.1039/C4TA04428B.

(3)   Zhang, H.; Hasa, I.; Passerini, S. Beyond Insertion for Na-Ion Batteries: Nanostructured Alloying and Conversion Anode Materials. *Advanced Energy Materials* **2018**, *8* (17), 1702582. https://doi.org/10.1002/aenm.201702582.

(4)   Hasa, I.; Hassoun, J.; Passerini, S. Nanostructured Na-Ion and Li-Ion Anodes for Battery Application: A Comparative Overview. *Nano Research* **2017**, *10* (12), 3942–3969. https://doi.org/10.1007/s12274-017-1513-7.

(5)   Dou, X.; Hasa, I.; Saurel, D.; Vaalma, C.; Wu, L.; Buchholz, D.; Bresser, D.; Komaba, S.; Passerini, S. Hard Carbons for Sodium-Ion Batteries: Structure, Analysis, Sustainability, and Electrochemistry. *Materials Today* **2019**, *23*, 87–104. https://doi.org/10.1016/j.mattod.2018.12.040.

(6)   Guo, S.; Yi, J.; Sun, Y.; Zhou, H. Recent Advances in Titanium-Based Electrode Materials for Stationary Sodium-Ion Batteries. *Energy & Environmental Science* **2016**, *9* (10), 2978–3006. https://doi.org/10.1039/C6EE01807F.

(7)   Liu, Y.; Yang, Y. Recent Progress of TiO_2 -Based Anodes for Li Ion Batteries. *Journal of Nanomaterials* **2016**, *2016*, 1–15. https://doi.org/10.1155/2016/8123652.

(8)   Wu, L.; Bresser, D.; Buchholz, D.; Giffin, G. A.; Castro, C. R.; Ochel, A.; Passerini, S. Unfolding the Mechanism of Sodium Insertion in Anatase TiO_2 Nanoparticles. *Advanced Energy Materials* **2015**, *5* (2), 1401142. https://doi.org/10.1002/aenm.201401142.

(9)   Hwang, J.-Y.; Myung, S.-T.; Sun, Y.-K. Sodium-Ion Batteries: Present and Future. *Chemical Society Reviews* **2017**, *46* (12), 3529–3614. https://doi.org/10.1039/C6CS00776G.

(10)   Pérez-Flores, J. C.; Baehtz, C.; Kuhn, A.; García-Alvarado, F. Hollandite-Type TiO_2 : A New Negative Electrode Material for Sodium-Ion Batteries. *J. Mater. Chem. A* **2014**, *2* (6), 1825–1833. https://doi.org/10.1039/C3TA13394J.

(11)   Louvain, N.; Henry, A.; Daenens, L.; Boury, B.; Stievano, L.; Monconduit, L. On the Electrochemical Encounter between Sodium and Mesoporous Anatase TiO_2 as a Na-Ion Electrode. *CrystEngComm* **2016**, *18* (23), 4431–4437. https://doi.org/10.1039/C5CE02598B.

(12)   Su, D.; Dou, S.; Wang, G. Anatase TiO_2 : Better Anode Material Than Amorphous and Rutile Phases of TiO_2 for Na-Ion Batteries. *Chemistry of Materials* **2015**, *27* (17), 6022–6029. https://doi.org/10.1021/acs.chemmater.5b02348.

(13)   Wang, W.; Liu, Y.; Wu, X.; Wang, J.; Fu, L.; Zhu, Y.; Wu, Y.; Liu, X. Advances of TiO_2 as Negative Electrode Materials for Sodium-Ion Batteries. *Advanced Materials Technologies* **2018**, *3* (9), 1800004. https://doi.org/10.1002/admt.201800004.

(14)   Wu, L.; Buchholz, D.; Bresser, D.; Gomes Chagas, L.; Passerini, S. Anatase TiO_2 Nanoparticles for High Power Sodium-Ion Anodes. *Journal of Power Sources* **2014**, *251*, 379–385. https://doi.org/10.1016/j.jpowsour.2013.11.083.

(15)   Wu, L.; Moretti, A.; Buchholz, D.; Passerini, S.; Bresser, D. Combining Ionic Liquid-Based Electrolytes and Nanostructured Anatase TiO_2 Anodes for Intrinsically Safer Sodium-Ion Batteries. *Electrochimica Acta* **2016**, *203*, 109–116. https://doi.org/10.1016/j.electacta.2016.03.124.

(16)   Tahir, M. N.; Oschmann, B.; Buchholz, D.; Dou, X.; Lieberwirth, I.; Panthöfer, M.; Tremel, W.; Zentel, R.; Passerini, S. Extraordinary Performance of Carbon-Coated Anatase TiO_2 as Sodium-Ion Anode. *Advanced Energy Materials* **2016**, *6* (4), 1501489. https://doi.org/10.1002/aenm.201501489.

(17) Wu, F.; Luo, R.; Xie, M.; Li, L.; Zhang, X.; Zhao, L.; Zhou, J.; Wang, K.; Chen, R. Facile Synthesis of Carbon-Mediated Porous Nanocrystallite Anatase TiO_2 for Improved Sodium Insertion Capabilities as an Anode for Sodium-Ion Batteries. *Journal of Power Sources* **2017**, *362*, 283–290. https://doi.org/10.1016/j.jpowsour.2017.07.050.

(18) Wang, B.; Zhao, F.; Du, G.; Porter, S.; Liu, Y.; Zhang, P.; Cheng, Z.; Liu, H. K.; Huang, Z. Boron-Doped Anatase TiO_2 as a High-Performance Anode Material for Sodium-Ion Batteries. *ACS Applied Materials & Interfaces* **2016**, *8* (25), 16009–16015. https://doi.org/10.1021/acsami.6b03270.

(19) Chen, J.; Ding, Z.; Wang, C.; Hou, H.; Zhang, Y.; Wang, C.; Zou, G.; Ji, X. Black Anatase Titania with Ultrafast Sodium-Storage Performances Stimulated by Oxygen Vacancies. *ACS Applied Materials & Interfaces* **2016**, *8* (14), 9142–9151. https://doi.org/10.1021/acsami.6b01183.

(20) Bella, F.; Muñoz-García, A. B.; Meligrana, G.; Lamberti, A.; Destro, M.; Pavone, M.; Gerbaldi, C. Unveiling the Controversial Mechanism of Reversible Na Storage in TiO_2 Nanotube Arrays: Amorphous versus Anatase TiO_2. *Nano Research* **2017**, *10* (8), 2891–2903. https://doi.org/10.1007/s12274-017-1656-6.

(21) Greco, G.; Passerini, S. Sodium Induced Morphological Changes of Carbon Coated TiO_2 Anatase Nanoparticles – High-Performance Materials for Na-Ion Batteries. *MRS Advances* **2020**, 1–9. https://doi.org/10.1557/adv.2020.259.

(22) Li, W.; Fukunishi, M.; Morgan, B. J.; Borkiewicz, O. J.; Chapman, K. W.; Pralong, V.; Maignan, A.; Lebedev, O. I.; Ma, J.; Groult, H.; Komaba, S.; Dambournet, D. A Reversible Phase Transition for Sodium Insertion in Anatase TiO_2. *Chemistry of Materials* **2017**, *29* (4), 1836–1844. https://doi.org/10.1021/acs.chemmater.7b00098.

(23) Greco, G.; Mazzio, K. A.; Dou, X.; Gericke, E.; Wendt, R.; Krumrey, M.; Passerini, S. Structural Study of Carbon-Coated TiO_2 Anatase Nanoparticles as High-Performance Anode Materials for Na-Ion Batteries. *ACS Applied Energy Materials* **2019**. https://doi.org/10.1021/acsaem.9b01101.

(24) González, J. R.; Zhecheva, E.; Stoyanova, R.; Nihtianova, D.; Markov, P.; Chapuis, R. R.; Alcántara, R.; Nacimiento, F.; Tirado, J. L.; Ortiz, G. F. A Fractal-like Electrode Based on Double-Wall Nanotubes of Anatase Exhibiting Improved Electrochemical Behaviour in Both Lithium and Sodium Batteries. *Physical Chemistry Chemical Physics* **2015**, *17* (6), 4687–4695. https://doi.org/10.1039/C4CP04572F.

(25) Xu, Z.-L.; Lim, K.; Park, K.-Y.; Yoon, G.; Seong, W. M.; Kang, K. Engineering Solid Electrolyte Interphase for Pseudocapacitive Anatase TiO_2 Anodes in Sodium-Ion Batteries. *Advanced Functional Materials* **2018**, *28* (29), 1802099. https://doi.org/10.1002/adfm.201802099.

(26) Kim, K.-T.; Ali, G.; Chung, K. Y.; Yoon, C. S.; Yashiro, H.; Sun, Y.-K.; Lu, J.; Amine, K.; Myung, S.-T. Anatase Titania Nanorods as an Intercalation Anode Material for Rechargeable Sodium Batteries. *Nano Letters* **2014**, *14* (2), 416–422. https://doi.org/10.1021/nl402747x.

(27) Wang, W.; Wu, M.; Han, P.; Liu, Y.; He, L.; Huang, Q.; Wang, J.; Yan, W.; Fu, L.; Wu, Y. Understanding the Behavior and Mechanism of Oxygen-Deficient Anatase TiO_2 toward Sodium Storage. *ACS Applied Materials & Interfaces* **2019**, *11* (3), 3061–3069. https://doi.org/10.1021/acsami.8b19288.

(28) Jung, K.-N.; Seong, J.-Y.; Kim, S.-S.; Lee, G.-J.; Lee, J.-W. One-Dimensional Nanofiber Architecture of an Anatase TiO_2 –Carbon Composite with Improved Sodium Storage Performance. *RSC Advances* **2015**, *5* (128), 106252–106257. https://doi.org/10.1039/C5RA14655K.

(29) Waychunas, G. A. Synchrotron Radiation XANES Spectroscopy of Ti in Minerals: Effects of Ti Bonding Distances, Ti Valence, and Site Geometry on Absorption Edge Structure. *American Mineralogist* **1987**, *72*, 89–101.

(30) Borghols, W. J. H.; Lützenkirchen-Hecht, D.; Haake, U.; Chan, W.; Lafont, U.; Kelder, E. M.; van Eck, E. R. H.; Kentgens, A. P. M.; Mulder, F. M.; Wagemaker, M. Lithium Storage in Amorphous

TiO₂ Nanoparticles. *Journal of The Electrochemical Society* **2010**, *157* (5), A582. https://doi.org/10.1149/1.3332806.

(31) Doyle, P. M.; Berry, A. J.; Schofield, P. F.; Mosselmans, J. F. W. The Effect of Site Geometry, Ti Content and Ti Oxidation State on the Ti K-Edge XANES Spectrum of Synthetic Hibonite. *Geochimica et Cosmochimica Acta* **2016**, *187*, 294–310. https://doi.org/10.1016/j.gca.2016.05.001.

(32) Farges, F.; Brown, G. E.; Rehr, J. J. Coordination Chemistry of Ti(IV) in Silicate Glasses and Melts: I. XAFS Study of Titanium Coordination in Oxide Model Compounds. *Geochimica et Cosmochimica Acta* **1996**, *60* (16), 3023–3038. https://doi.org/10.1016/0016-7037(96)00144-5.

(33) Liu, Y.; Zhao, F.; Li, J.; Li, Y.; McLeod, J. A.; Liu, L. Influence of Crystal Phase on TiO₂ Nanowire Anodes in Sodium Ion Batteries. *Journal of Materials Chemistry A* **2017**, *5* (37), 20005–20013. https://doi.org/10.1039/C7TA05852G.

(34) Farges, F.; Brown, G. E.; Rehr, J. J. Ti K -Edge XANES Studies of Ti Coordination and Disorder in Oxide Compounds: Comparison between Theory and Experiment. *Physical Review B* **1997**, *56* (4), 1809–1819. https://doi.org/10.1103/PhysRevB.56.1809.

(35) Xiong, H.; Slater, M. D.; Balasubramanian, M.; Johnson, C. S.; Rajh, T. Amorphous TiO₂ Nanotube Anode for Rechargeable Sodium Ion Batteries. *The Journal of Physical Chemistry Letters* **2011**, *2* (20), 2560–2565. https://doi.org/10.1021/jz2012066.

(36) Lin, F.; Liu, Y.; Yu, X.; Cheng, L.; Singer, A.; Shpyrko, O. G.; Xin, H. L.; Tamura, N.; Tian, C.; Weng, T.-C.; Yang, X.-Q.; Meng, Y. S.; Nordlund, D.; Yang, W.; Doeff, M. M. Synchrotron X-Ray Analytical Techniques for Studying Materials Electrochemistry in Rechargeable Batteries. *Chemical Reviews* **2017**, *117* (21), 13123–13186. https://doi.org/10.1021/acs.chemrev.7b00007.

(37) Dong, C.; Vayssieres, L. In Situ/Operando X-ray Spectroscopies for Advanced Investigation of Energy Materials. *Chemistry – A European Journal* **2018**, *24* (69), 18356–18373. https://doi.org/10.1002/chem.201803936.

(38) Yamamoto, T. Assignment of Pre-Edge Peaks in K-Edge x-ray Absorption Spectra of 3d Transition Metal Compounds: Electric Dipole or Quadrupole? *X-Ray Spectrometry* **2008**, *37* (6), 572–584. https://doi.org/10.1002/xrs.1103.

(39) Jackson, W. E.; Farges, F.; Yeager, M.; Mabrouk, P. A.; Rossano, S.; Waychunas, G. A.; Solomon, E. I.; Brown, G. E. Multi-Spectroscopic Study of Fe(II) in Silicate Glasses: Implications for the Coordination Environment of Fe(II) in Silicate Melts. *Geochimica et Cosmochimica Acta* **2005**, *69* (17), 4315–4332. https://doi.org/10.1016/j.gca.2005.01.008.

(40) Mei, S.; Jafta, C. J.; Lauermann, I.; Ran, Q.; Kärgell, M.; Ballauff, M.; Lu, Y. Porous Ti₄O₇ Particles with Interconnected-Pore Structure as a High-Efficiency Polysulfide Mediator for Lithium-Sulfur Batteries. *Advanced Functional Materials* **2017**, *27* (26), 1701176. https://doi.org/10.1002/adfm.201701176.

(41) Gorgoi, M.; Svensson, S.; Schäfers, F.; Öhrwall, G.; Mertin, M.; Bressler, P.; Karis, O.; Siegbahn, H.; Sandell, A.; Rensmo, H.; Doherty, W.; Jung, C.; Braun, W.; Eberhardt, W. The High Kinetic Energy Photoelectron Spectroscopy Facility at BESSY Progress and First Results. *Nuclear Instruments and Methods in Physics Research Section A: Accelerators, Spectrometers, Detectors and Associated Equipment* **2009**, *601* (1–2), 48–53. https://doi.org/10.1016/j.nima.2008.12.244.

(42) Schäfers, F.; Mertin, M.; Gorgoi, M. KMC-1: A High Resolution and High Flux Soft x-Ray Beamline at BESSY. *Review of Scientific Instruments* **2007**, *78* (12), 123102. https://doi.org/10.1063/1.2808334.

(43) Gorgoi, M.; Schäfers, F.; Svensson, S.; Mårtensson, N. Relative Sub-Shell Photoionization Cross-Sections of Nickel Metal Determined by Hard X-Ray High Kinetic Energy Photoemission. *Journal of Electron Spectroscopy and Related Phenomena* **2013**, *190*, 153–158. https://doi.org/https://doi.org/10.1016/j.elspec.2013.01.004.

(44) Comin, F.; Incoccia, L.; Mobilio, S. Glitches Compensation in EXAFS Data Collection. *Journal of Physics E: Scientific Instruments* **1983**, *16* (1), 83–86. https://doi.org/10.1088/0022-3735/16/1/016.

(45) Henke, B. L.; Gullikson, E. M.; Davis, J. C. X-Ray Interactions: Photoabsorption, Scattering, Transmission, and Reflection at E=50-30000 EV, Z=1-92. *Atomic Data and Nuclear Data Tables* **1993**, *Vol. 54* (No. 2), 181–342.

(46) Yang, K.-S.; Lu, Y.-R.; Hsu, Y.-Y.; Lin, C.-J.; Tseng, C.-M.; Liou, S. Y. H.; Kumar, K.; Wei, D.-H.; Dong, C.-L.; Chen, C.-L. Plasmon-Induced Visible-Light Photocatalytic Activity of Au Nanoparticle-Decorated Hollow Mesoporous TiO_2 : A View by X-Ray Spectroscopy. *The Journal of Physical Chemistry C* **2018**, *122* (12), 6955–6962. https://doi.org/10.1021/acs.jpcc.8b00205.

(47) Yogi, C.; Kojima, K.; Hashishin, T.; Wada, N.; Inada, Y.; Della Gaspera, E.; Bersani, M.; Martucci, A.; Liu, L.; Sham, T.-K. Size Effect of Au Nanoparticles on TiO_2 Crystalline Phase of Nanocomposite Thin Films and Their Photocatalytic Properties. *The Journal of Physical Chemistry C* **2011**, *115* (14), 6554–6560. https://doi.org/10.1021/jp110581j.

(48) Angelomé, P. C.; Andrini, L.; Calvo, M. E.; Requejo, F. G.; Bilmes, S. A.; Soler-Illia, G. J. A. A. Mesoporous Anatase TiO_2 Films: Use of Ti K XANES for the Quantification of the Nanocrystalline Character and Substrate Effects in the Photocatalysis Behavior. *The Journal of Physical Chemistry C* **2007**, *111* (29), 10886–10893. https://doi.org/10.1021/jp069020z.

(49) Matsuo, S.; Sakaguchi, N.; Wakita, H. Pre-Edge Features of Ti K-Edge X-Ray Absorption Near-Edge Structure for the Local Structure of Sol-Gel Titanium Oxides. *Analytical Sciences* **2005**, *21* (7), 805–809. https://doi.org/10.2116/analsci.21.805.

(50) Luca, V.; Djajanti, S.; Howe, R. F. Structural and Electronic Properties of Sol−Gel Titanium Oxides Studied by X-Ray Absorption Spectroscopy. *The Journal of Physical Chemistry B* **1998**, *102* (52), 10650–10657. https://doi.org/10.1021/jp981644k.

(51) Oliveira, M. M.; Schnitzler, D. C.; Zarbin, A. J. G. (Ti,Sn)O_2 Mixed Oxides Nanoparticles Obtained by the Sol−Gel Route. *Chemistry of Materials* **2003**, *15* (9), 1903–1909. https://doi.org/10.1021/cm0210344.

(52) Richtmyer, F. K.; Barnes, S. W.; Ramberg, E. The Widths of the L -Series Lines and of the Energy Levels of Au(79). *Physical Review* **1934**, *46* (10), 843–860. https://doi.org/10.1103/PhysRev.46.843.

(53) Wasserman, S. R. The Analysis of Mixtures: Application of Principal Component Analysis to XAS Spectra. *Le Journal de Physique IV* **1997**, *7* (C2), C2-203-C2-205. https://doi.org/10.1051/jp4/1997163.

(54) Kim, W. B.; Choi, S. H.; Lee, J. S. Quantitative Analysis of Ti−O−Si and Ti−O−Ti Bonds in Ti−Si Binary Oxides by the Linear Combination of XANES. *J. Phys. Chem. B* **2000**, *104* (36), 8670–8678. https://doi.org/https://doi.org/10.1021/jp000042+.

(55) Ajiboye, B.; Akinremi, O. O.; Jürgensen, A. Experimental Validation of Quantitative XANES Analysis for Phosphorus Speciation. *Soil Science Society of America Journal* **2007**, *71* (4), 1288–1291. https://doi.org/10.2136/sssaj2007.0007.

(56) Webb, S. M. SIXPack a Graphical User Interface for XAS Analysis Using IFEFFIT. *Physica Scripta* **2005**, 1011. https://doi.org/10.1238/Physica.Topical.115a01011.

(57) Wu, Z. Y.; Ouvrard, G.; Gressier, P.; Natoli, C. R. Ti and O K Edges for Titanium Oxides by Multiple Scattering Calculations: Comparison to XAS and EELS Spectra. *Physical Review B* **1997**, *55* (16), 10382–10391. https://doi.org/10.1103/PhysRevB.55.10382.

(58) Luca, V. Comparison of Size-Dependent Structural and Electronic Properties of Anatase and Rutile Nanoparticles. *The Journal of Physical Chemistry C* **2009**, *113* (16), 6367–6380. https://doi.org/10.1021/jp808358v.

(59) Brydson, R.; Sauer, H.; Engel, W.; Thomass, J. M.; Zeitler, E.; Kosugi, N.; Kuroda, H. Electron Energy Loss and X-Ray Absorption Spectroscopy of Rutile and Anatase: A Test of Structural Sensitivity. *Journal of Physics: Condensed Matter* **1989**, *1* (4), 797–812. https://doi.org/10.1088/0953-8984/1/4/012.

(60) Li, J.; Liu, J.; Sun, Q.; Banis, M. N.; Sun, X.; Sham, T.-K. Tracking the Effect of Sodium Insertion/Extraction in Amorphous and Anatase TiO_2 Nanotubes. *The Journal of Physical Chemistry C* **2017**, *121* (21), 11773–11782. https://doi.org/10.1021/acs.jpcc.7b01106.

(61) Ling, L.; Bai, Y.; Li, Y.; Ni, Q.; Wang, Z.; Wu, F.; Wu, C. Quick Activation of Nanoporous Anatase TiO_2 as High-Rate and Durable Anode Materials for Sodium-Ion Batteries. *ACS Applied Materials & Interfaces* **2017**, *9* (45), 39432–39440. https://doi.org/10.1021/acsami.7b13927.

(62) Petkov, V.; Holzhu, G. Atomic-Scale Structure of Amorphous TiO_2 by Electron, X-Ray Diffraction and Reverse Monte Carlo Simulations. *Journal of Non-Crystalline Solids* **1998**, *231*, 17–30.

(63) Hoang, V. V.; Zung, H.; Trong, N. H. B. Structural Properties of Amorphous TiO_2 Nanoparticles. *The European Physical Journal D* **2007**, *44* (3), 515–524. https://doi.org/10.1140/epjd/e2007-00186-5.

(64) Zhang, H.; Chen, B.; Banfield, J. F.; Waychunas, G. A. Atomic Structure of Nanometer-Sized Amorphous TiO_2. *Physical Review B* **2008**, *78* (21). https://doi.org/10.1103/PhysRevB.78.214106.

(65) Di Valentin, C.; Pacchioni, G.; Selloni, A. Reduced and N-Type Doped TiO_2 : Nature of Ti^{3+} Species. *The Journal of Physical Chemistry C* **2009**, *113* (48), 20543–20552. https://doi.org/10.1021/jp9061797.

(66) De Angelis, F.; Di Valentin, C.; Fantacci, S.; Vittadini, A.; Selloni, A. Theoretical Studies on Anatase and Less Common TiO_2 Phases: Bulk, Surfaces, and Nanomaterials. *Chemical Reviews* **2014**, *114* (19), 9708–9753. https://doi.org/10.1021/cr500055q.

(67) Rudola, A.; Saravanan, K.; Devaraj, S.; Gong, H.; Balaya, P. $Na_2Ti_6O_{13}$: A Potential Anode for Grid-Storage Sodium-Ion Batteries. *Chemical Communications* **2013**, *49* (67), 7451. https://doi.org/10.1039/c3cc44381g.

(68) Sánchez-Camacho, P.; Romero-Ibarra, I. C.; Duan, Y.; Pfeiffer, H. Thermodynamic and Kinetic Analyses of the CO_2 Chemisorption Mechanism on Na_2TiO_3 : Experimental and Theoretical Evidences. *The Journal of Physical Chemistry C* **2014**, *118* (34), 19822–19832. https://doi.org/10.1021/jp504922e.

(69) Akimoto, J.; Takei, H. Synthesis and Crystal Structure of $NaTi_8O_{13}$. *Journal of Solid State Chemistry* **1991**, *90* (1), 147–154. https://doi.org/10.1016/0022-4596(91)90180-P.

(70) Akimoto, J.; Takei, H. Synthesis and Crystal Structure of $NaTi_2O_4$: A New Mixed-Valence Sodium Titanate. *Journal of Solid State Chemistry* **1989**, *79* (2), 212–217. https://doi.org/10.1016/0022-4596(89)90268-5.